Growth of equiaxed dendritic crystals settling in an undercooled melt, Part 2: Internal solid fraction

A. Badillo, D. Ceynar, C. Beckermann*

Department of Mechanical and Industrial Engineering, The University of Iowa, 2402 Seamans Center, Iowa City, IA 52242, USA

Communicated by G.B. McFadden
Available online 21 September 2007

Abstract

Experiments are conducted to measure the internal solid fraction evolution of equiaxed dendritic crystals that are freely growing and settling in an undercooled melt using the transparent model alloy succinonitrile–acetone. The internal solid fraction is determined from the measured settling speed and crystal envelope shape and size. Depending on the melt undercooling and acetone concentration, the internal solid fraction is found to vary between 0.55 and 0.1. In all experiments, the internal solid fraction decreases continually during settling. Based on heat and solute balances, a model is developed for predicting the internal solid fraction evolution under convective conditions. Nusselt and Sherwood number correlations are obtained that allow for the calculation of the thermal and solutal boundary layer thicknesses at the crystal envelope. The measured and predicted internal solid fraction evolutions are found to be in good agreement.

1. Introduction

In Part 1 of this study [1], dendrite tip growth of equiaxed crystals settling in an undercooled melt was investigated experimentally using the transparent model alloy succinonitrile (SCN)–acetone. The results provide not only for additional experimental validation of standard dendritic growth theory [2–5], but also for increased insight into the effect of flow on dendrite tip growth. In the present paper (Part 2), the same experiments are used to explore the development of the dendritic solid behind the tips, internal to the crystal envelope. As discussed in more detail below, the envelope of a dendritic crystal is defined as a particular closed surface that connects the tips of all actively growing branches (see Fig. 1). Hence, the evolution of the size and shape of the envelope is solely governed by dendrite tip growth. Knowledge of tip growth kinetics is, however, not sufficient to fully characterize the growth of

an equiaxed crystal since the dendrite arms can have different thicknesses and some (inactive) arms internal to the envelope may not be growing at all. Therefore, it has become customary to define an internal solid fraction, ε_i, which is simply the solid volume divided by the envelope volume, as an additional quantity to describe a dendritic crystal [6–10]. Note that the internal solid fraction of dendritic crystals should be distinguished from the regular solid fraction in the mushy zone of solidifying alloys. Inside mushy zones, the melt is usually not undercooled, and the solid fraction can be determined from standard microsegregation models (e.g., Lever rule, Scheil equation). On the other hand, the evolution of the internal solid fraction is governed by heat and solute transport from the dendritic crystal into the undercooled melt surrounding it. The concept of an internal solid fraction has proven to be very useful in the modeling of the grain structure formation in the casting of metal alloys [9–11].

While several theoretical models for the internal solid fraction evolution in dendritic growth into an undercooled melt have been proposed [7,8,12,13], their direct experimental

---

*Corresponding author. Tel.: +1 319 335 5681; fax: +1 319 335 5669.
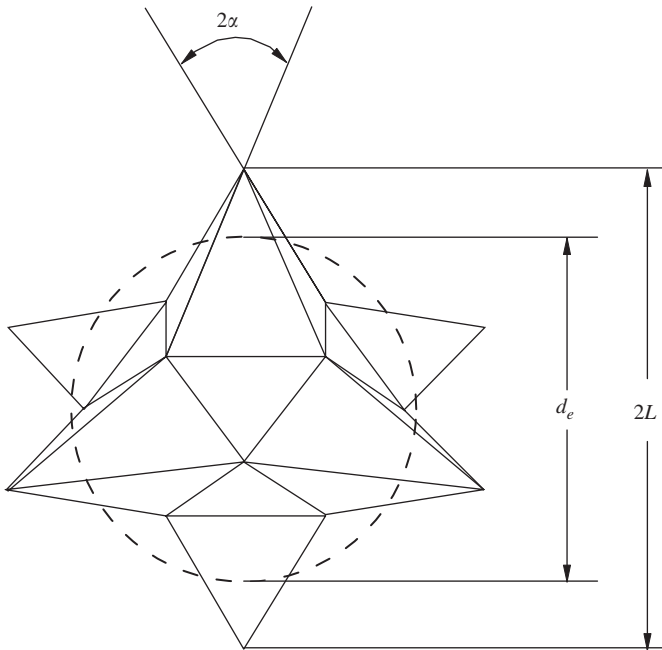*E-mail address:* becker@engineering.uiowa.edu (C. Beckermann).

Fig. 1. Schematic of the equiaxed crystal envelope geometry; the dashed circle indicates the envelope volume equivalent sphere.

validation has been difficult. This is undoubtedly related to the fact that the morphology of a dendritic crystal is extremely complex, at a sub-millimeter scale, and constantly changing. Li and Beckermann [14] estimated the solid volume of dendritic crystals using images from the microgravity experiments of Glicksman and coworkers involving pure SCN [15]. These measurements were found to be in good agreement with a simple model based on heat diffusion from the crystal envelope into the uniformly undercooled melt. The results indicate that at small times, but in the steady tip growth regime, the internal solid fraction varies inversely with time, t, according to $\varepsilon_i \sim R/v_t t$, where R and v_t are the dendrite tip radius and velocity, respectively. The internal solid fraction decreases initially, because a dendritic crystal develops from a small solid seed with $\varepsilon_i = 1$. At large times, the internal solid fraction is predicted to reach a constant value given by $\varepsilon_i = \Omega$, where Ω is the dimensionless melt undercooling. All other validation efforts have been indirect. Examples include measurement of the temperature recalescence associated with nucleation of equiaxed grains in castings or measurement of the fraction of interdendritic phases in fully solidified alloys (e.g., Refs. [6,7,12,16]).

The present experiments involving settling of equiaxed dendritic crystals in an undercooled melt offer a unique opportunity to study the evolution of the internal solid fraction. By measuring the settling speed and the crystal envelope shape and size, the internal solid fraction can readily be determined. Considerable previous experimental work has resulted in the availability of a correlation for the drag coefficient of equiaxed dendrites [17]. Furthermore, the solid and liquid densities of SCN–acetone alloys have also been measured to a high degree of accuracy [18]. As opposed to the investigation of Li and Beckermann [14]

involving microgravity data, the internal solid fraction in the present experiments is likely to be affected by the flow of the melt relative to the settling crystal. Thus, the primary objective of the present study is to understand the effect of melt flow on heat and solute transport from equiaxed crystals growing in an undercooled melt. The measurements are used to develop a model to predict the internal solid fraction evolution in the presence of melt convection. The only previous such model was not validated experimentally [13]. All details of the experimental setup and measurement procedures are described in Part 1 of this study.

2. Measurement of internal solid fraction

The equiaxed crystal envelope geometry used in the present study is the same as in de Groh III et al. [17] and is illustrated in Fig. 1. It consists of six orthogonal square pyramids that are joined together at their base. Thus, the center volume has six square surfaces, coinciding with the bases of the pyramids, and eight equilateral triangular surfaces. The tips of the six pyramids coincide with the tips of the six primary dendrite arms of an equiaxed crystal. The distance from the tips of two opposing pyramids is equal to twice the measured average primary dendrite arm length, $\bar{L}$ (see Fig. 12 in Part 1). The tips of the secondary dendrite arms are located at the edges of the pyramids. The pyramid angle, α, is defined as the angle between the primary dendrite arm axis and a straight line connecting the tips of the secondary arms. An average value of this angle was measured from the images acquired for each experiment and is listed in Table 1. The uncertainty in the angle measurement was $\pm 5°$. It can be seen from Table 1 that in all experiments the average pyramid angle was within two degrees of $31°$.

The length $\bar{L}$ and angle α completely define the envelope and allow for the calculation of its volume, V_e, and surface area, A_e, according to Ref. [17]:

$$V_e = (t_1^2 t_2 + 5t_1^3/6)\bar{L}^3 = f_1 \bar{L}^3 \qquad (1)$$

and

$$A_e = \left(6t_1\sqrt{2t_2^2 + t_1^2/4} + t_1^2\sqrt{3}\right)\bar{L}^2 = f_2 \bar{L}^2, \qquad (2)$$

where $t_1 = \tan\alpha/(1 + \tan\alpha)$ and $t_2 = 1/[2(1 + \tan\alpha)]$. The radius, r_e, of the envelope volume equivalent sphere (see Fig. 1) is given by

$$r_e = [3f_1/(4\pi)]^{1/3}\bar{L} = f_3 \bar{L}. \qquad (3)$$

Note that the geometric factors f_1, f_2, and f_3 are constant for a given angle α; for example, for $\alpha = 30°$, they are equal to 0.0833, 1.30, and 0.271, respectively. If the envelope were taken as a sphere of radius $r_e = \bar{L}$, the three factors would be equal to $4\pi/3$, 4π, and 1, respectively.

The measured envelope volume equivalent sphere diameter, $d_e = 2r_e$, is plotted as a function of time in Fig. 2. Results are shown for each of the eight experiments

summarized in Table 1. In all cases, the equivalent diameter increases linearly with time. Thus, the equivalent envelope growth velocity, given by $v_e = dr_e/dt$, is a constant during an experiment. These velocities are also shown in Fig. 2 and listed in Table 1. The envelope growth velocity is constant since the average primary dendrite tip growth velocity, $\bar{v}_t = d\bar{L}/dt$, is constant in the present experiments, as explained in Part 1.

Having defined the crystal envelope, the internal solid fraction can be obtained from a force balance on the settling crystal. Neglecting acceleration effects, a balance of the drag and buoyancy forces on the crystal can be written as

$$\frac{1}{2}\rho_l U^2 \left(\frac{\pi d_e^2}{4}\right)\frac{C_D}{KS_e} = gV_s(\rho_s - \rho_l), \tag{4}$$

where ρ_l and ρ_s are liquid and solid densities, respectively, U is the measured settling speed, g ($= 9.81\,\mathrm{m^2/s}$) is the gravitational acceleration, and V_s is the solid volume. The drag coefficient C_D corresponds to that of a solid sphere of diameter d_e and is calculated from a correlation developed in Ref. [19] for small to intermediate Reynolds numbers:

$$C_D = \frac{24}{Re}(1 + 0.15 Re^{0.687}), \tag{5}$$

where the Reynolds number is defined as $Re = Ud_e/v$ and v is the kinematic melt viscosity. As shown in Table 1, for the range of settling speeds and envelope volume equivalent sphere diameters measured in the present experiments, and using the properties in Table 3 of Part 1, the Reynolds number of the settling equiaxed crystals varied from 0.4 to 10. The equiaxed dendrite settling speed ratio, KS_e, in Eq. (4) is given by the following correlation developed by de Groh III et al. [17] based on settling experiments involving a range of scaled (such that the Reynolds numbers are in the same range as in the present experiments), but realistically shaped models of dendrites:

$$KS_e = 1.26 \log_{10}\left(\frac{\psi}{0.163}\right) \times \frac{2\beta^2 + 3(1 - \tanh(\beta)/\beta)}{2\beta^2(1 - \tanh(\beta)/\beta)}, \tag{6}$$

where $\psi = \pi d_e^2/A_e$ is the envelope sphericity and $\beta = r_e/\sqrt{K_e}$ is the ratio of the envelope radius to the square root of the permeability of the dendritic structure inside

of the envelope. The first term on the right-hand side of Eq. (6) accounts for the effect of the non-spherical shape of the envelope on the drag. For a given angle α, the sphericity is a constant (e.g., $\psi = 0.712$ for $\alpha = 30°$). The second term accounts for the fact that the envelope is porous and melt can flow through the internal dendritic structure. However, based on an estimate of the permeability, $\beta \gg 10$ and the second term can be taken as equal to unity. The above correlation was validated in Ref. [17] by comparing measured and predicted settling speeds of equiaxed dendritic crystals in a variety of transparent and metallic alloys.

Introducing the internal solid fraction as $\varepsilon_i = V_s/V_e$, Eq. (4) can finally be re-written as:

$$\varepsilon_i = \frac{3U^2 C_D}{4d_e KS_e g}\left(\frac{\rho_l}{\rho_s - \rho_l}\right). \tag{7}$$

This equation allows for the calculation of the internal solid fraction from the settling speed, U, and the average primary dendrite arm length (since $d_e = 2f_3\bar{L}$). These two measured quantities are plotted as a function of time in Figs. 3 and 12 in Part 1. All properties, including the densities as a function of temperature and solute concentration, are taken from Table 3 in Part 1. The internal solid fractions obtained in this manner are shown as solid lines in Fig. 3 for each of the eight experiments in Table 1. It can be seen that the internal solid fraction generally ranges from about 0.55 to 0.1. Higher internal solid fractions were not observed because tracking of the crystals started only when they had already grown a well-developed dendritic structure. In all eight experiments, the internal solid fraction decreases with time during settling. However, in some experiments (e.g., 1, 2, and 8) the decrease is less than 0.05, while in others (e.g., 7) it is as high as 0.45. Referring to the envelope diameters plotted in Fig. 2, it can be seen that larger crystals (e.g., in experiments 3, 6, and 8) often have a lower internal solid fraction than smaller crystals (e.g., in experiment 7), but there is no direct correlation. The internal solid fraction measurements shown in Fig. 3 are analyzed theoretically in the next section.

The estimated uncertainty in the internal solid fraction from the above settling calculations is equal to about 15%. Most of that uncertainty comes from the difficulty to

Table 1
Experimental conditions and summary of envelope and settling variables

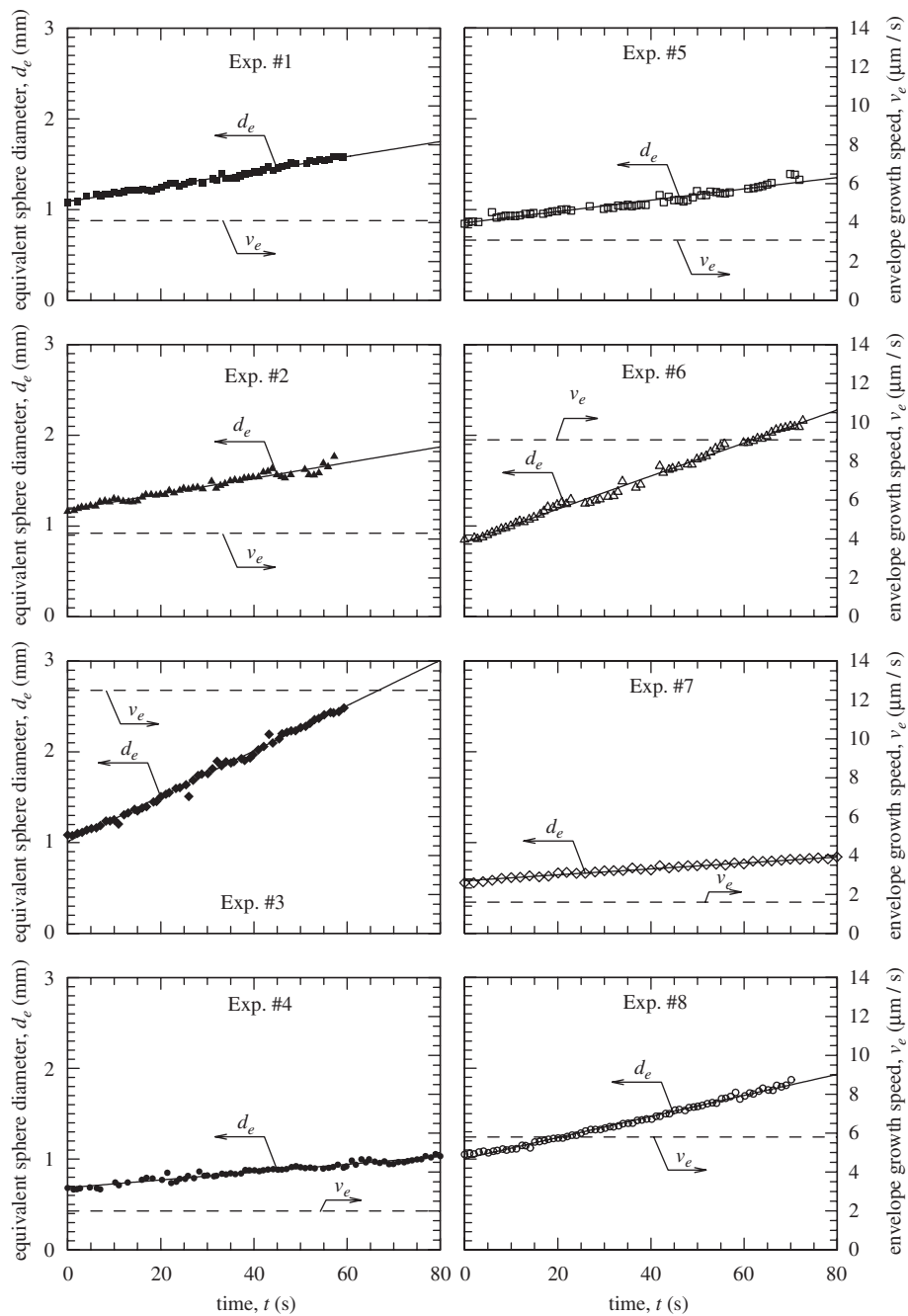| Exp.	C_0 (wt%)	ΔT (K)	U^i (mm/s)	U^f (mm/s)	α (deg)	V_e (µm/s)	Re^i	Re^f
1	1.08	0.53	3.47	5.93	30	4.1	1.43	3.94
2	1.08	0.54	4.05	7.38	30	4.3	1.79	5.21
3	1.08	0.84	3.01	8.11	31	12.5	1.25	9.55
4	1.40	0.47	2.64	4.23	29	2.0	0.69	1.62
5	2.96	0.82	2.62	4.20	31	3.1	0.85	2.15
6	2.96	1.3	2.08	5.57	32	9.1	0.68	4.91
7	3.97	0.75	1.91	1.94	32	1.6	0.41	0.61
8	3.97	1.23	1.74	4.33	32	5.8	0.70	3.27

Fig. 2. Measured envelope volume equivalent sphere diameters as a function of time (symbols) and parabolic fit (solid lines), and corresponding envelope growth velocities (straight dashed lines).

accurately measure the average angle α between the primary dendrite arm axis and a straight line connecting the tips of the secondary branches. However, since a constant value of α is taken for each experiment, and variations in α between the experiments are small (see Table 1), this uncertainty does not affect the general nature of the internal solid fraction variations with time and the differences between the values of the internal solid fraction among the various experiments shown in Fig. 3. It should also be noted that another choice for the envelope geometry, for example one that is less form fitting, would

result in different values for the internal solid fraction. Again, this does not affect the nature of the internal solid fraction variations in Fig. 3.

3. Model development and comparison with experimental results

In the following, a model is developed to predict the internal solid fraction during settling of equiaxed dendritic crystals in an undercooled melt. The model is based on heat and solute balances. The measurements are used to develop
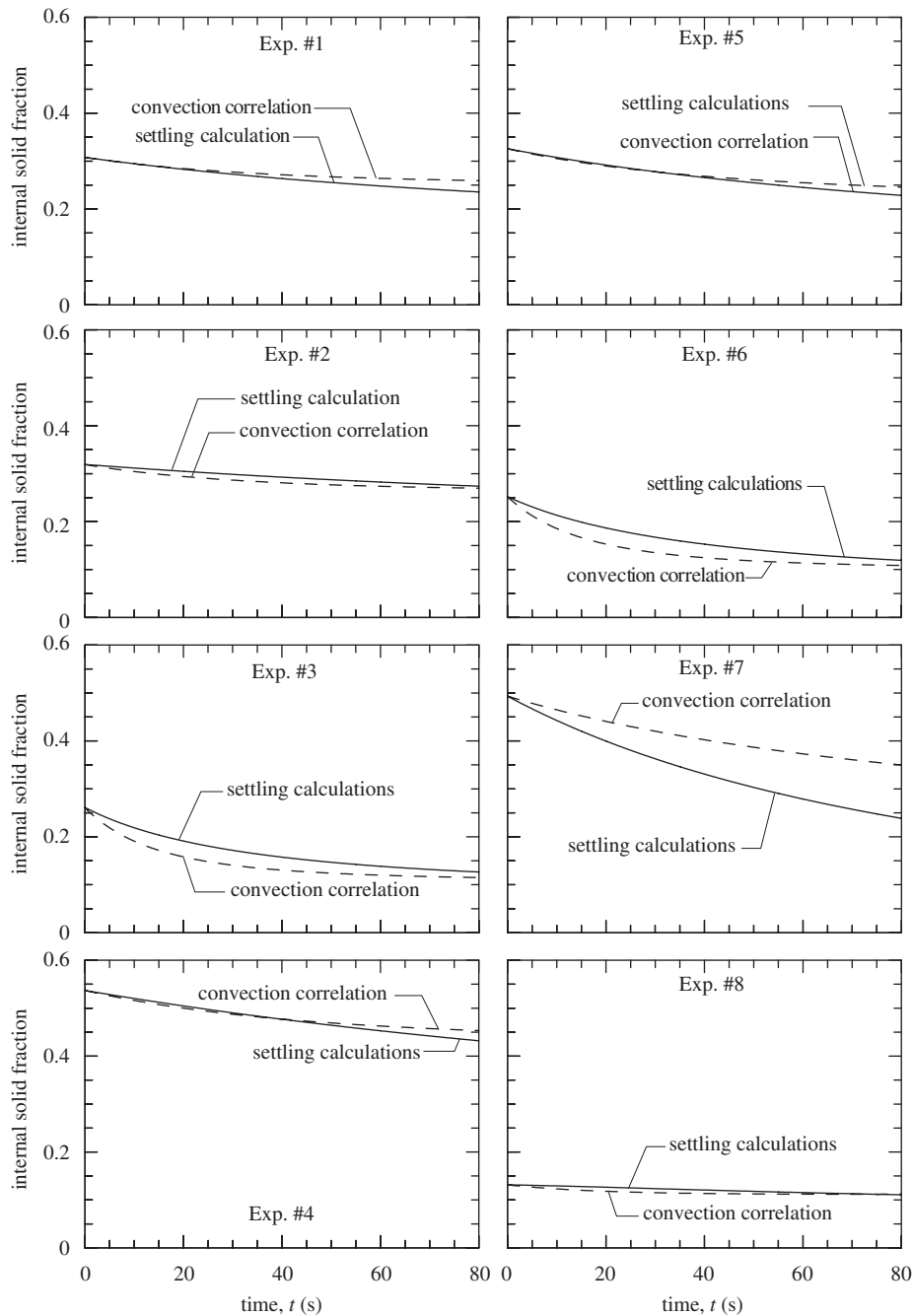
Fig. 3. Comparison of the internal solid fraction variations determined from the settling measurements (solid lines) and predicted by the convection model (dashed lines).

a convection heat and mass transfer correlation for equiaxed crystals. The model predictions are then compared to the results presented in the previous section.

3.1. Heat and solute balances

The latent heat and solute rejected during the growth of an equiaxed crystal are transported from the crystal envelope into the undercooled melt, as illustrated in Fig. 4. Hence, heat and solute balances can be written,

respectively, as

$$\rho_s L_f \frac{dV_s}{dt} = A_e k_1 \frac{T^* - T_0}{\delta_T} \tag{8}$$

and

$$\rho_s C_1^*(1-k)\frac{dV_s}{dt} = A_e \rho_1 D_1 \frac{C_1^* - C_0}{\delta_C}, \tag{9}$$

where L_f is the latent heat of fusion, k is the partition coefficient, k_1 is the liquid thermal conductivity, D_1 is the liquid mass diffusivity, and T_0 and C_0 are the constant
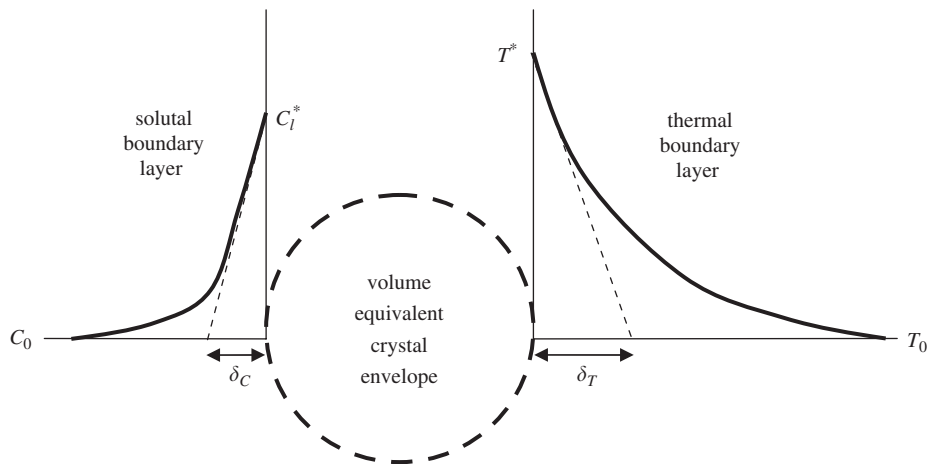
Fig. 4. Schematic illustration of the thermal and solutal boundary layers at the equiaxed crystal envelope.

far-field temperature and solute concentration of the undercooled melt, respectively. The finely dispersed solid–liquid mixture inside the crystal envelope is assumed to be in equilibrium and at a temperature T^* and liquid solute concentration C_l^*. This temperature and solute concentration are assumed to be constant during the present settling experiments. The thermal and solutal boundary layer thicknesses, δ_T and δ_C, are also shown in Fig. 4. They are defined such that the average heat and solute gradients at the envelope surface are given by $(T^* - T_0)/\delta_T$ and $(C_l^* - C_0)/\delta_C$, respectively.

Eqs. (8) and (9) are rewritten as follows. Since $\varepsilon_i = V_s/V_e$, the solidification rate can be expanded as

$$\frac{\mathrm{d}V_s}{\mathrm{d}t} = \varepsilon_i \frac{\mathrm{d}V_e}{\mathrm{d}t} + V_e \frac{\mathrm{d}\varepsilon_i}{\mathrm{d}t}. \tag{10}$$

Eq. (10) states that the solid volume can change due to a change in the envelope volume at a constant internal solid fraction and due to a change in the internal solid fraction at a constant envelope volume. The change in the envelope volume can be expressed in terms of the equivalent envelope growth velocity as

$$\frac{1}{V_e} \frac{\mathrm{d}V_e}{\mathrm{d}t} = \frac{3}{r_e} v_e. \tag{11}$$

Recall that v_e is constant in the present experiments (see Fig. 2). The dimensionless thermal and solutal undercoolings are defined, respectively, as

$$\Omega_T = \frac{T^* - T_0}{L_f/c_l} \quad \text{and} \quad \Omega_C = \frac{C_l^* - C_0}{C_l^*(1 - k)}, \tag{12}$$

where c_l is the liquid specific heat. Introducing Eqs. (10)–(12) into Eqs. (8) and (9), and taking $\rho_s \approx \rho_l$, the heat and solute balances become finally

$$\frac{\mathrm{d}\varepsilon_i}{\mathrm{d}t} = \frac{f_4 \alpha_l}{\delta_T r_e} \Omega_T - \frac{3v_e}{r_e} \varepsilon_i \tag{13}$$

and

$$\frac{\mathrm{d}\varepsilon_i}{\mathrm{d}t} = \frac{f_4 D_l}{\delta_C r_e} \Omega_C - \frac{3v_e}{r_e} \varepsilon_i, \tag{14}$$

where $\alpha_l = k_l/(\rho_l c_l)$ is the liquid thermal diffusivity and $f_4 = f_2 f_3/f_1$. For the present envelope geometry with $\alpha = 30°$, $f_4 = 4.21$; if the envelope were taken as a sphere of radius $r_e = \bar{L}$, $f_4 = 3$. A comparison of the above two equations yields

$$\frac{\Omega_C}{\Omega_T} = Le \frac{\delta_C}{\delta_T}, \tag{15}$$

where Le is the Lewis number, given by $Le = \alpha_l/D_l$. Eq. (15) must be valid at all times.

The dimensionless thermal and solutal undercoolings in Eqs. (13) and (14) are not known a priori. Recognizing that the total imposed melt undercooling, ΔT, is the sum of the thermal and solutal undercoolings, the following additional relation results (see Part 1):

$$\Delta T = \frac{L_f}{c_l} \Omega_T + \frac{k \Delta T_0 \Omega_C}{1 - (1 - k)\Omega_C}, \tag{16}$$

where $\Delta T_0 = mC_0(1 - 1/k)$ is the equilibrium freezing temperature range, in which m is the liquidus slope. Given expressions for δ_T and δ_C (see below), and using the measured equivalent envelope radii and growth velocities, r_e and v_e (see Fig. 2), the set of equations given by Eqs. (13), (14), and (16) is now closed and can be solved for the internal solid fraction as a function of time, as well as for the dimensionless thermal and solutal undercoolings (which are constant). Instead of using the measured r_e and v_e, the equivalent envelope radius and growth velocity could also be obtained from a theoretical prediction of the dendrite tip growth velocity, since $v_e = \mathrm{d}r_e/\mathrm{d}t = f_3 \bar{v}_t$. Recall from Part 1 that for the present settling experiments the average dendrite tip growth velocity, $\bar{v}_t$, is accurately predicted by the standard free dendritic growth theory for alloys [2–5].

3.2. Quasi-steady growth

Before proceeding, it is useful to examine the solution of the above set of equations in the long-time limit. The quasi-steady growth regime is defined here as the limit where

$d\varepsilon_i/dt = 0$. Then, the heat and solute balances given by Eqs. (13) and (14) can be solved directly for the internal solid fraction to yield

$$\varepsilon_i = \frac{f_4 \alpha_l}{3 v_e \delta_T} \Omega_T = \frac{f_4 D_l}{3 v_e \delta_C} \Omega_C. \tag{17}$$

These two equations are generally valid in the quasi-steady growth regime. However, they must be interpreted carefully. If the boundary layer thicknesses were given by

$$\delta_T = (f_4/3)\alpha_l/v_e \quad \text{and} \quad \delta_C = (f_4/3)D_l/v_e, \tag{18}$$

Eq. (17) would yield that the internal solid fraction is equal to the dimensionless undercoolings, i.e., $\varepsilon_i = \Omega_T = \Omega_C$. Note that $f_4/3 = 1.4$ for the present envelope geometry with $\alpha = 30°$, and $f_4/3 = 1$ for a spherical envelope. This is essentially the result obtained by Rappaz and Thevoz [8], Li and Beckermann [14], and others. Even though Eq. (18) may be appealing from a theoretical point of view, since the diffusion boundary layer thickness at a moving front is commonly taken to be proportional to the ratio of the diffusivity to the growth velocity, it is *not* generally valid, even in the quasi-steady growth regime. This is explained in more detail next.

The fact that the diffusion boundary layer thickness at a moving front is proportional to the ratio of the diffusivity to the growth velocity, as in Eq. (18), is only true in the limit of large growth Péclet numbers. The thermal and solutal envelope growth Péclet numbers are defined as $Pe_T = v_e r_e/\alpha_l$ and $Pe_C = v_e r_e/D_l$, respectively [16]. On the other hand, in the limit of small growth Péclet numbers, an analytical solution of the diffusion equation around a sphere reveals that the boundary layer thicknesses are given by $\delta_T = \delta_C = r_e$, which is independent of the growth velocity. According to Eq. (17), this would result in the internal solid fraction continually decreasing as the envelope radius increases during (quasi-steady) growth, which contradicts the seemingly general statement that $\varepsilon_i = \Omega_T = \Omega_C = \text{const.}$. Based on the data in Table 1 and Fig. 2, the thermal Péclet number in the present experiments is always much less than unity, i.e. $Pe_T \ll 1$, while the solutal Péclet number varies from about 0.35 to 15, with the average being about unity. While an analytical solution is available for the quasi-steady boundary layer thickness that is valid for any growth Péclet number [16], it is still only valid for a sphere growing in a purely diffusive environment. In the present settling experiments, the boundary layer thicknesses can be expected to strongly depend on the melt velocity relative to the crystal, especially since the flow Reynolds number can be as large as 10 (see Table 1). Neither Eq. (18) nor the expression $\delta_T = \delta_C = r_e$ accounts for any convection effects. Convection effects can be dominant even if the growth Péclet number is of the order of unity.

Based on this discussion, it must be concluded that the boundary layer thickness in Eq. (17) can take any value, depending on the nature of the heat and solute transport from the crystal envelope into the undercooled melt, and

that $\varepsilon_i = \Omega_T = \Omega_C$ is not generally valid. The presence of the equivalent envelope growth velocity, v_e, in Eq. (17) simply indicates that the internal solid fraction is, as expected, a function of how fast the envelope grows. It does not reveal anything about the boundary layer thicknesses. They must be obtained from separate relations. Eq. (18) should be used only if (i) the growth is quasi-steady, (ii) the envelope growth Péclet numbers are large, and (iii) the growth occurs in a purely diffusive environment (no flow). None of these conditions are satisfied in the present experiments. The fact that the growth in the present experiments is generally not in the quasi-steady regime can be seen in Fig. 3 by noting some of the large measured internal solid fraction variations with time during settling.

3.3. Determination of the thermal and solutal boundary layer thicknesses

The thermal and solutal boundary layer thicknesses in the present settling experiments are obtained from the measured internal solid fractions in a trial-and-error fashion, as explained below. It is assumed that the boundary layer thicknesses do not depend on the envelope growth velocity, v_e, as may be expected in the diffusion limit. This assumption is valid if the envelope growth Péclet numbers are relatively small (see above) or if the heat and solute transport from the settling equiaxed crystals is dominated by convection effects. Additional justification is provided below. With this assumption, the boundary layer thicknesses can be expressed in terms of Nusselt and Sherwood number correlations of the following form:

$$Nu = d_e/\delta_T = cRe^{1/2}Pr^{1/3}, \quad \text{and}$$
$$Sh = d_e/\delta_C = cRe^{1/2}Sc^{1/3}, \tag{19}$$

where $Pr = v/\alpha_l$ and $Sc = v/D_l = Pr\,Le$ are the Prandtl and Schmidt numbers, respectively, and c is a constant. These kinds of relations are used extensively to correlate heat and mass transfer data for forced convection from bodies of arbitrary shape [20]. Due to the limited availability of experimental data, the exponents on the Reynolds, Prandtl, and Schmidt numbers are assumed to be known. The exponent of $\frac{1}{2}$ on Re has been found to work well for small to intermediate Reynolds numbers, regardless of the shape of the body. The exponent of $\frac{1}{3}$ on Pr and Sc is only valid for those numbers that are equal to or greater than unity, which is the case in the present experiments (see Table 3 in Part 1), but not for liquid metals. The constant c depends on the shape of the body, but can be expected to be the same in all of the present experiments, since the envelope sphericity is approximately constant (see above). All of these constants can be expected to be the same for both heat and solute transport. The above correlations are not valid for $Re \rightarrow 0$, which is consistent with the assumption that the diffusion limit is not important in the present experiments.

The correlations given by Eq. (19) imply that

$$\frac{\delta_C}{\delta_T} = Le^{-1/3}. \tag{20}$$

Note that substitution of Eq. (20) into Eq. (15) yields the interesting result that $\Omega_C/\Omega_T = Le^{2/3}$. Eq. (19) also indicates that the boundary layer thicknesses vary according to $\delta_T \sim d_e^{1/2} U^{-1/2}$ and $\delta_C \sim d_e^{1/2} U^{-1/2}$. In the present experiments, the equivalent envelope diameter increases linearly with time, i.e. $d_e \sim t$ (see Fig. 2). Furthermore, the settling speed also increases linearly with time, i.e. $U \sim t$ (see Fig. 3 in Part 1). Therefore, the boundary layer thicknesses can be assumed to be constant. The above relations then allow for a relatively easy determination of the boundary layer thickness from the measured internal solid fractions, because for each experiment only one value needs to be obtained. The following trial-and-error procedure was adopted. Guessing a value for δ_C (or δ_T), the set of equations provided in Section 3.1 [i.e., Eqs. (13), (14) and (16)] and Eq. (20) were solved numerically using the measured internal solid fraction from the settling calculations at $t = 0$ as the initial condition. The internal solid fraction was stepped in time until the conclusion of the experiment ($t \approx 80$ s). The predicted internal solid fraction at that time was then compared to the measured value from the settling calculations at the same time. A new value for the boundary layer thickness was guessed, and the above steps were repeated, until the final internal solid fractions agreed.

The thermal and solutal boundary layer thicknesses obtained in this manner are listed for each experiment in Table 2. Focusing on the solutal boundary layer thickness (since $\delta_T/\delta_C = Le^{1/3} \approx 4.5$), it can be seen that all δ_C are within 20% of 0.24 mm, except for experiment 7 where $\delta_C = 0.58$ mm. Considering that ν_e varies by more than a factor of seven among the experiments, it is clear that an expression of the form of Eq. (18), i.e. $\delta_C \sim D_l/\nu_e$, would not work in correlating the measured boundary layer thicknesses. The reason that δ_C is so similar among most experiments is related to $\delta_C \sim d_e^{1/2} U^{-1/2}$; this product is not only independent of time, but also of the same magnitude in most experiments. A larger crystal has a thicker boundary layer, but a larger crystal also settles faster,

which causes the boundary layer to become thinner. The two effects approximately cancel each other in the same manner for all crystals. The reason why δ_C is so different for experiment 7 is not entirely clear, but could be related to the fact that this crystal had the smallest envelope diameters and growth velocity (see Table 1). For such a small crystal, the present measurements become less accurate. However, the crystal in experiment 4 was only slightly larger, and its solutal boundary layer thickness is close to 0.24 mm.

Table 2 also lists the undercoolings resulting from the solution of the governing set of equations, using the measured boundary layer thicknesses. The dimensionless thermal undercooling is generally much smaller than the dimensionless solutal undercooling, since $\Omega_T = Le^{-2/3}\Omega_C = 0.05\Omega_C$. However, this does not mean that the thermal undercooling is negligibly small in the present experiments. Converting the dimensionless undercoolings to the dimensional undercoolings ΔT_T and ΔT_C in Kelvin, Table 2 shows that, for the first three experiments with the smallest solute concentration, the ratio $\Delta T_T/\Delta T_C$ is as high as 0.38. In other words, the thermal undercooling is a significant fraction of the total imposed melt undercooling, ΔT. This ratio reduces to about 0.11 for the last two experiments with the largest solute concentration.

As the final step in the model development, the boundary layer thicknesses obtained from the heat and solute balances are used to determine a value for the constant c in the Nusselt and Sherwood number correlations given by Eq. (19). The measured solutal boundary layer thickness and equivalent envelope diameter were substituted into $Sh = d_e/\delta_C$ to obtain a measured Sherwood number. As above, the measured settling speed and d_e were substituted into $Re = Ud_e/\nu$ to obtain a measured Reynolds number. Fig. 5 shows a plot of the measured Sherwood versus Reynolds number variations for each of the eight experiments. As expected, they all follow the same trend, except for experiment 7. The data in Fig. 5, weighed equally for each experiment, were fit to the correlation given by Eq. (19), resulting in $c = 0.312$. The final correlation is included in Fig. 5 as a thick solid line. It can be seen to predict the measured Sherwood numbers to within better than 20%, except for experiment 7. The value of the constant c obtained in this manner is of a reasonable

Table 2
Boundary layer thicknesses and undercoolings obtained from the convection model

| Exp.	C_0 (wt%)	ΔT (K)	δ_T (mm)	δ_C (mm)	Ω_T	Ω_C	ΔT_T (K)	ΔT_C (K)	$\Delta T_T/\Delta T_C$
1	1.08	0.53	1.14	0.256	0.0063	0.126	0.145	0.384	0.38
2	1.08	0.54	0.912	0.204	0.0064	0.128	0.148	0.392	0.38
3	1.08	0.84	1.00	0.224	0.0095	0.190	0.219	0.619	0.35
4	1.40	0.47	0.974	0.218	0.0047	0.0939	0.109	0.361	0.30
5	2.96	0.82	1.15	0.258	0.0044	0.0886	0.103	0.716	0.14
6	2.96	1.3	1.05	0.235	0.0068	0.135	0.156	1.14	0.14
7	3.97	0.75	2.59	0.580	0.0032	0.0638	0.0739	0.675	0.11
8	3.97	1.23	1.30	0.290	0.0051	0.101	0.117	1.11	0.11
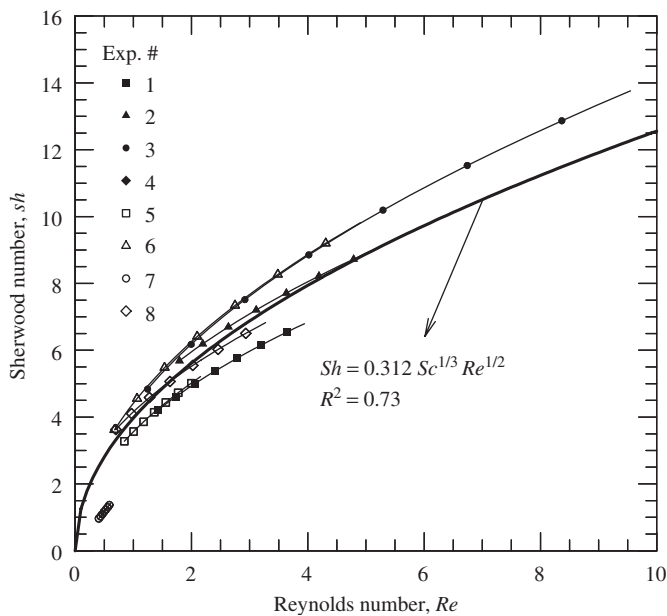
Fig. 5. Variation of the measured Sherwood number with Reynolds number (symbols connected by thin lines) and correlation representing the best fit for all experiments (thick solid line).

magnitude when compared to such values in other convection heat and mass transfer correlations found in the literature [20].

3.4. Comparison of measured and predicted internal solid fractions

The predicted internal solid fraction variations from the present model, using the above convection correlations with $c = 0.312$, are compared to the measurements in Fig. 3 for all eight experiments. The measured initial internal solid fraction from the settling calculations is used to start the numerical integration of the governing equations. Overall, good agreement can be observed over the entire time period of the experiments. The final values of the internal solid fraction do not agree perfectly, because the convection correlation was used to calculate the boundary layer thicknesses rather than the values listed in Table 2. As expected from the previous discussion, the largest disagreement occurs for experiment 7.

4. Conclusions

Measurements of the internal solid fraction evolution of equiaxed dendritic SCN–acetone crystals that are settling in an undercooled melt are performed. The experiments cover a relatively large range of melt undercoolings and solute concentrations. The internal solid fraction is determined from the measured settling speed and the measured size and shape of the crystal envelope. It generally decreases during settling and ranges from about 0.55 to 0.1. Based on heat and solute balances, a model is developed to predict the internal solid fraction evolution.

The convective heat and solute transport rates from the envelope into the undercooled melt are characterized by thermal and solutal boundary layer thicknesses. It is found that during an experiment the boundary layer thicknesses are constant, despite significant crystal size and settling speed variations. By matching measured and predicted final internal solid fractions, values for the boundary layer thicknesses are determined and correlated. The resulting Nusselt and Sherwood number correlations constitute the main finding of this study. Using the correlations, the measured internal solid fraction variations are predicted well for all but one experiment.

Taken together, Parts 1 and 2 completely characterize the growth of equiaxed dendritic crystals in the presence of convection. The models presented in this study allow for the calculation of the dendrite tip growth velocities, the settling speed, and the internal solid fraction evolution. However, care should be taken in applying the models to conditions that are significantly different from the present experiments, as already mentioned in Part 1. For example, the Nusselt and Sherwood number correlations presented in this paper would require some modification before they can be applied to metal alloys. Nonetheless, the present study contributes significantly to the development and validation of models for the prediction of the grain structure of metal alloy castings.

References

[1] A. Badillo, D. Ceynar, C. Beckermann, J. Crystal Growth (2007), doi:10.1016/j.jcrysgro.2007.09.018.
[2] J. Lipton, M.E. Glicksman, W. Kurz, Mater. Sci. Eng. 65 (1984) 57.
[3] J. Lipton, M.E. Glicksman, W. Kurz, Metall. Trans. A 18A (1987) 341.
[4] J. Lipton, W. Kurz, R. Trivedi, Acta Metall. 35 (1987) 957.
[5] R. Trivedi, W. Kurz, Int. Mater. Rev. 39 (1994) 49.
[6] I. Dustin, W. Kurz, Z. Metallkd 77 (1986) 265.
[7] M. Rappaz, P.H. Thevoz, Acta Metall. 35 (1987) 1487.
[8] M. Rappaz, P.H. Thevoz, Acta Metall. 35 (1987) 2929.
[9] M. Rappaz, Int. Mater. Rev. 34 (1989) 93.
[10] C. Beckermann, C.Y. Wang, Ann. Rev. Heat Transfer 6 (1995) 115.
[11] C. Beckermann, Int. Mater. Rev. 47 (2002) 243.
[12] C.Y. Wang, C. Beckermann, Metall. Trans. 24A (1993) 2787.
[13] C.Y. Wang, C. Beckermann, Metall. Mater. Trans. 27A (1996) 2754.
[14] Q. Li, C. Beckermann, Phys. Rev. E 57 (1998) 3176.
[15] M.B. Koss, J.C. LaCombe, L.A. Tennenhouse, M.E. Glicksman, E.A. Winsa, Metall. Mater. Trans. 30A (1999) 3177.
[16] M.A. Martorano, C. Beckermann, Ch.-A. Gandin, Metall. Mater. Trans. 34A (2003) 1657.
[17] H.C. de Groh III, P.D. Weidman, D. Zakhem, S. Ahuja, C. Beckermann, Metall. Trans. 24B (1993) 749.
[18] D.L. Ceynar, C. Beckermann, J. Crystal Growth 222 (2001) 380.
[19] A.R. Khan, J.F. Richardson, Chem. Eng. Comm. 62 (1987) 135.
[20] F.P. Incropera, D.P. DeWitt, T.L. Bergman, A.S. Lavine, Fundamentals of Heat and Mass Transfer, sixth ed, Wiley, 2007.